PORE FORMATION IN SOLID

P. S. Wei * **S. Y. Hsiao** **S. S. Hsieh**

Department of Mechanical and Electro-Mechanical Engineering
National Sun Yat-Sen University
Kaohsiung, Taiwan 80424, R.O.C.

ABSTRACT

The shapes of a growing or decaying bubble entrapped by a solidification front are predicted in this work. The bubble results from supersaturation of a dissolved gas in the liquid ahead of the solidification front. Pore formation and its shape in solid are one of the most critical factors affecting properties, microstructure, and stresses in materials. In this study, the bubble and pore shapes entrapped in solid can be described by a three-dimensional phase diagram, obtained from perturbation solutions of Young-Laplace equation governing the tiny bubble shape in the literature. The predicted growth and entrapment of a microbubble as a pore in solid are found to agree with experimental data. This work thus provides a realistic prediction of the general growth of the pore shape as a function of different working parameters.

Keywords: Pore formation, Bubble entrainment, Phase change, Solidification defect, Porosity.

1. INTRODUCTION

Porosity is one of the serious defects commonly occurring in engineering applications such as welding [1-4] and castings [5-7], materials and manufacturing processing [8,9]. However, metals containing significant pores also have characteristics, which are different from those of bulk metals, such as an inherently low density and a large surface area. Therefore, these metals can be utilized as lightweight materials, catalysts, vibration and acoustic energy damping materials, impact energy absorption materials, and so on [10]. Understanding pore formation and controlling its behavior therefore are challenging topics to be investigated.

Pores can be formed by different types of mechanisms, such as they can be resulted by solute rejection from the solid phase during solidification [11-14], gas entrapped in the molten layer [15], liquid enclosing the vapor phase [3], and insufficient feeding of space during solidification shrinkage [5,6] or interdendritic growth [1,6]. Pore formation due to solute rejection from the solidification front results from supersaturation nucleation. Pores can be in sizes of micrometers. The gas entrapment in the molten layer or liquid enclosing vapor phase is related to hydrodynamic instabilities of the free surface. The liquid enclosing vapor phase due to collapse of the liquid phase is usually encountered in keyhole mode welding. Pores are in sizes of millimeters. Shrinkage porosity may occur because of difference in densities between solid and liquid during solidification from the lack of liquid metal feeding. Interdendritic porosity occurs when gas bubbles are formed or entrapped between dendrite arms in the solidification substructure.

Since morphology of the pores is complicated in the mushy zone of alloys, theoretical models in castings are focused on predicting percentage porosity or an average equivalent spherical radius [5,6]. In this approach, the temperature and liquid fraction are calculated from heat conduction equation subject to the lever rule or Scheil's equation to relate liquid fraction by temperature. The liquid pressure can be determined by substituting the Darcy's law or the momentum equations into the continuity equation. In view of the assumed sphere-shaped pore, the gas pressure in the pore can be simply found by using the Young-Laplace equation. The percentage porosity and sphere-shaped pore thus is determined from conservation of dissolvable gas. The actual pore size, however, was not calculated.

A determination of the pore shape, however, is important, since it is responsible for mechanical properties such as fatigue, tensile strength and limited elongation. For example, fatigue strength of the final product depends on the length of the pore even though the pore volume is the same. On the other hand, the pore shape exhibits many interesting phenomena [16-25]. For example, in view of impurity accumulated near the solidification front, Geguzin and Dzuba [24] observed and proposed that a two-zone structure of a gas-saturated liquid characterized by a well-typed, semi-closed, closed pore, boundary containing crystalized gas- saturated liquid and gas bubble resulted. A stepwise processing pressure change can result in either a regular transient change in pore diameter, or a complete termi-

* Corresponding author (pswei@mail.nsysu.edu.tw)

DOI : 10.1017/jmech.2012.1
Copyright © 2012 The Society of Theoretical and Applied Mechanics, R.O.C.
https://doi.org/10.1017/jmech.2012.1 Published online by Cambridge University Press

nation of pore growth [16]. The coupling of the bubble with the solidification front can also be found to cause oscillations [9].

Except for the interdendritic porosity constrained by the primary and secondary dendrites in microstructures, pore formation can be modeled by considering a growing or decaying bubble entrapped by the solidification front in supersaturated or supercooled liquids. In order to predict realistic pore formation in solid, transient deformation of the bubble cap above the solidification front and pore in the solid is required. The transient model for a bubble entrapped in solid as a pore is still limited. Furthermore, a systematical and detailed determination of the pore shape should account for mass, momentum, energy and concentration for the growth of a bubble trapped in solid [26,27]. Since gas in liquid accumulated at the bubble cap in the course of solidification, mass transport to the bubble was enhanced and gas pressure in the bubble was increased. A satisfaction of momentum balance led to a decrease of cap radius.

Recently, a general three-dimensional shape or phase diagrams of a microbubble on a solid surface was found by applying perturbation solutions with small Bond numbers of Young-Laplace equation [28]. The phase diagrams are found to be divided into three regions, depending on if the microbubble surface contains the inflection point or neck. The general growth, departure and entrapment of a microbubble thus can be described by path lines on diagrams by adjusting the apex and base radii, where the time-dependent apex radius is related to the transient variations of the surrounding, liquid and capillary pressures. Introducing the time-dependent pressures, a realistic and general shape of the bubble can be determined from the phase diagram, leading to a realistic pore shape in the solid. This becomes the objective of this work.

In this work, the bubble entrapped as a pore in a supersaturated liquid is treated. The bubble and pore shapes entrapped in solid can be described by a three-dimensional phase diagram by utilizing perturbation solutions of Young-Laplace equation governing the tiny bubble shape in the literature. The predicted growth and entrapment of a microbubble in solid can be extended to a general behavior of bubble and pore dynamics in the future.

2. SYSTEM MODEL AND ANALYSIS

A pore in solid resulted from entrapment of a microbubble on a solidification front at a depth h_B below the free surface is illustrated in Fig. 1. The shape of the bubble cap beyond the solidification front is determined by the Young-Laplace equation, which governs the normal stress balance between gas, capillary and liquid pressures. The solidification front is at location $s(t)$ measured from the initial solidification front. Inclination angle ϕ, and axial coordinate $\tilde{z}$ measured from the apex toward the base are also introduced. The apex radius is $R(0)$, while the contact angle and base radius are denoted by ϕ_B and r_B, respectively. The corresponding apex radius, contact angle and base radius at the initial state are $\tilde{R}_0$, ϕ_{B0} and r_{B0}, respectively. The shape of a bubble can be characterized by three regions [28]. That is, a bubble shape in region I is referred to the bubble surface containing the apex point. The bubble shape in region II is for the surface further containing the inflection point. The bubble shape in region III is for the bubble surface containing a neck. The major assumptions made are the following:

1. The model system is axisymmetric.
2. The bubble is in a microscale, leading to apply available perturbation solutions of a lumped microbubble shape.
3. The system is static. Hence, tangential and normal viscous stresses in the liquid are neglected. Liquid pressure is hydrostatic pressure.

With the above assumptions, the bubble shape in region I is described by

$$r = L\left(\sin\phi - \frac{\pi-\phi}{2} + \frac{1}{2}\sqrt{(\pi-\phi)^2 - \frac{8}{3}L^2Bo}\right) + \frac{1}{3}L^3Bo\left(\frac{2}{\pi-\phi} - \cos^2\phi\tan\frac{\phi}{2}\right) \tag{1}$$

$$z = L\left[1-\cos\phi + \left(\frac{\pi-\phi}{2}\right)^2 - \frac{\pi-\phi}{4}\sqrt{(\pi-\phi)^2 - \frac{8}{3}L^2Bo}\right] + \frac{2}{3}L^3Bo\left\{\frac{1}{2}\left(1+\cos\phi-\cos^2\phi+2\ln\cos\frac{\phi}{2}\right) + \ln\left(\frac{1}{2(\pi-\phi)}\sqrt{(\pi-\phi)^2 - \frac{8}{3}L^2Bo} + \frac{1}{2}\right)\right\} \tag{2}$$

where dimensionless radial and axial coordinates are normalized by the initial bubble radius, $r = \tilde{r}/\tilde{R}_0$, $z = \tilde{z}/\tilde{R}_0$. The Bond number $Bo \equiv \rho_\ell g\tilde{R}_0^2/\sigma$, where ρ_ℓ, g and σ stand for liquid density, gravitational acceleration, and surface tension, respectively. The solutions for the bubble shapes in regions II and III can be found in the article of [28]. The dimensionless bubble width at the inclination angle of $\pi/2$ in Eqs. (1) and (2) is

$$L = R(0) + \frac{1}{6}Bo + o(Bo^2) \tag{3}$$

where dimensionless bubble width and apex radius are $L = \tilde{L}/\tilde{R}_0$ $R(0) = \tilde{R}(0)/\tilde{R}_0$, respectively. The radius of curvature at the apex can be determined by Young-Laplace equation

$$R(0) = \frac{2}{2 + p_g - p_{g0} + Bo\left[s - (z_{B0} - z_B)\right]} \tag{4}$$

where dimensionless gas pressure $p_g \equiv \tilde{p}_g\tilde{R}_0/\sigma$, p_{g0} is the gas pressure at the initial time, z_B and z_{B0} are apex heights at time t and initial time, respectively.

https://doi.org/10.1017/jmech.2012.1 Published online by Cambridge University Press

The gas pressure in Eq. (4) is given by [27]

$$p_g = \frac{V(0)}{V(t)} e^{\int_0^t N dt'} \left[p_{g0} - KC_\infty Bo \int_0^t \left(\frac{NV(\tau)}{V(0)} e^{-\int_0^\tau N(t')\,dt'} \right) d\tau \right] \tag{5}$$

where dimensionless Henry's constant $K = \tilde{K} / \tilde{R}_u \tilde{T}$, mass transfer coefficient $h_D = \tilde{h}_D \tilde{R}_0 / \tilde{D}$, initial solute content $C_\infty = \tilde{C}_\infty \tilde{R}_u \tilde{T} / \rho g \tilde{R}_0$, parameter governing mass transfer across the bubble cap $N \equiv h_D \pi r_B^2 / VK$, time $t = \tilde{t}\tilde{D} / \tilde{R}_0^2$, and volume $V = \tilde{V} / \tilde{R}_0^3$ includes the volumes of the bubble cap and pore in the solid. Quantities $\tilde{R}_u$, $\tilde{T}$ and $\tilde{D}$ are, respectively, dimensional universal gas constant, temperature and solute diffusivity. Geometric consideration gives (see Fig. 1)

$$\frac{dr_B}{ds} = \frac{1}{\tan(\pi - \phi_B)} \tag{6}$$

which indicates the continuity of the slope between the bubble cap and pore in the solid at the level of the solidification front. The radius of the bubble cap at the same level as the solidification front is

$$r_B = r(\phi_B) \tag{7}$$

The cap height on the axisymmetric axis is

$$z(\phi_B) = z_B \tag{8}$$

The pore volume in Eq. (5) yields

$$V = V_w + V_c \tag{9}$$

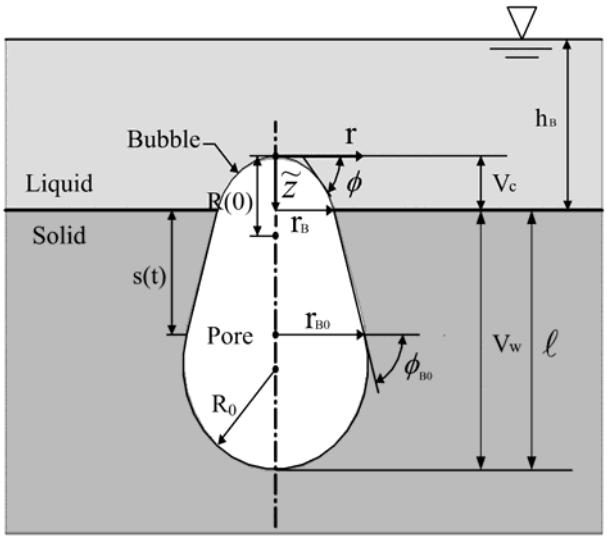


Fig. 1. Schematic sketch of physical model

where the volumes below and above the solidification front are, respectively, V_w and V_c, given by

$$V_w = V_{w0} + \int_0^t \pi r_B^2 \frac{ds}{dt'} dt' \tag{10}$$

$$V_c = \int_0^{\phi_B} \pi r^2 \frac{dz}{d\phi} d\phi \tag{11}$$

3. SOLUTION PROCEDURE

The solution procedure is as follows:

1. Select initial conditions for a spherical bubble with contact angle ϕ_{B0}, dimensionless radius $R_0 = 1$, and specified solidification rate, and values of independent dimensionless parameters,
2. Calculate contact angle r_B from Eq. (6), and L from Eq. (3),
3. Determine contact angle ϕ_B from Eqs. (1) and (7),
4. Calculate cap height z_B from Eq. (2),
5. Calculate pore volume V from Eqs. (9) ~ (11),
6. Calculate gas pressure P_g from Eq. (5),
7. Calculate cap radius $R(0)$ from Eq. (4),
8. Go to step 2 for the next time.

4. RESULTS AND DISCUSSION

In this work, typical independent dimensionless parameters and variables are estimated from a microbubble in a typical size of $10^{-4} - 10^{-6}$m nucleated on the solidification front with a solidification rate $10^{-5} - 10^{-6}$m/s in cooling water containing a dissolved carbon dioxide gas around 0.001 ~ 0.3wt% and solute diffusivity of $10^{-7} - 10^{-9}$m^2/s. Surface tension of water is 0.076N/m, mass transfer coefficient is 10^{-6}m/s, Henry's constant is $10^6 - 10^8$Pa/wt%. Therefore, Bond number $Bo = 0.00149$, dimensionless initial gas pressure $P_{g0} = 1$, initial contact angle $\phi_{B0} = 120°$, Henry's constant $K = 10$, solidification rate $ds/dt = 0.04$, solute gas concentration far away from the solidification front $C_\infty = 50$.

Equation (4) indicates that the apex radius is determined by the surrounding, liquid and gas pressures. The development of the bubble or pore shapes thus is strongly affected by the variation of the apex radius with time. This is a consequence of the time-dependent gas pressure governed by Eq. (5) which is a function of mass transfer from the liquid to bubble. Precisely speaking, gas pressure is a function of initial gas pressure and solute gas content, Henry's constant, mass transfer coefficient, solute diffusivity, Bond number, and the total volume of the bubble cap in liquid and pore in solid, *etc*. Furthermore, time-dependent apex radius can also be affected by time-dependent hydrostatic pressure, as a result of the instantaneous locations of the cap apex and solidification front.

https://doi.org/10.1017/jmech.2012.1 Published online by Cambridge University Press

Figure 2 shows the displacement of the solidification front with time correlated from the measurement conducted by Wei *et al*. [25] in the solidification of water containing carbon dioxide at a cold temperature of –25°C. With the given solidification rate, the predicted contact angle as a function of time agrees with experimental data [25], as shown in Fig. 3. It can be seen that there exists a long period of time at the contact angle around $\pi/2$. The reason for this is that the moving distance of the solidification front is large when the contact angle approaches $\pi/2$. The significant deviation between the prediction and measurement starts to occur near the contact angle around $\pi/2$. The errors induced by measurements may be one of the factors affecting the deviation. A comparison between the measured and predicted cap radius at the solidification front as a function of time is shown in Fig. 4. It can be seen that the agreement is quite good. The maximum cap radius apparently corresponds to the contact angle at $\pi/2$.

A predicted development of a pore from entrainment of a bubble with an initial contact angle of 120° on the solidification front in the course of solidification is shown in Fig. 5. The horizontal solid lines represent the solid-liquid interfaces at different times. It can be seen that the pore length grows with time. Provided that solute diffusivity is 10^{-9}m^2/s and initial bubble radius is 10^{-5}m, the dimensional time for the bubble entirely enclosed in the solid is 27s. Figure 6 shows the effect of the initial Bond number on the pore shape. An increase in the initial Bond number results in an early bubble entrapment. This can be attributed to a decrease in surface tension, which reduces the radius of the bubble to balance gas pressure in the bubble.

Different developments of the pore shape, as presented in previous Figs. 5 and 6, can be simply and generally described by a three-dimensional dimensionless phase diagram, as shown in Fig. 7. For a given initial Bond number, the transient growth of the pore length, ℓ, is uniquely determined by the time-dependent dimensionless apex radius and cap radius. The time- dependent apex radius is an important variable which reflects the transient effects of the atmospheric, liquid and capillary pressure. It can be seen that the development of the pore shape in previous Fig. 5 is described by the process from states labeled *A* to *C*. In the course of solidification, the pore length increases with time. As the cap radius reduces to zero, the bubble cap is sunk to solid and a closed pore is formed. Similarly, that in previous Fig. 6 is referred to the process from states *E* to *G*. Even though the initial state is the same, namely, the same dimensionless cap and apex radii at the initial state, the process from states *E* to *G* has a greater value of apex radius than the process from states *A* to *C*. Therefore, different processes for the developments of the pore shapes can be described by varying the apex radius, which is determined by the time-dependent surrounding, liquid and capillary pressures.

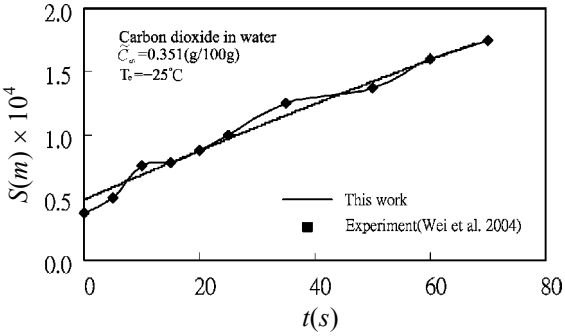


Fig. 2 The measured and correlated displacement of the solidification front versus time

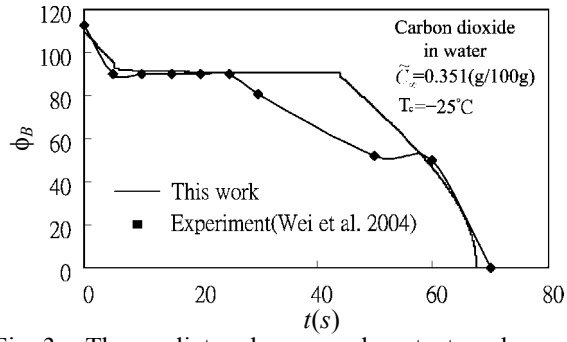


Fig. 3 The predict and measured contact angle as a function of time

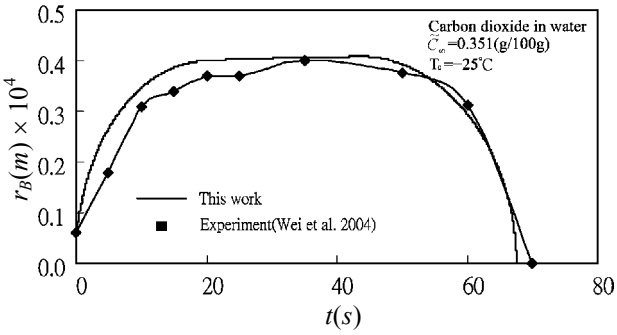


Fig. 4 The predicted and measured cap radius at the solidification front as a function of time

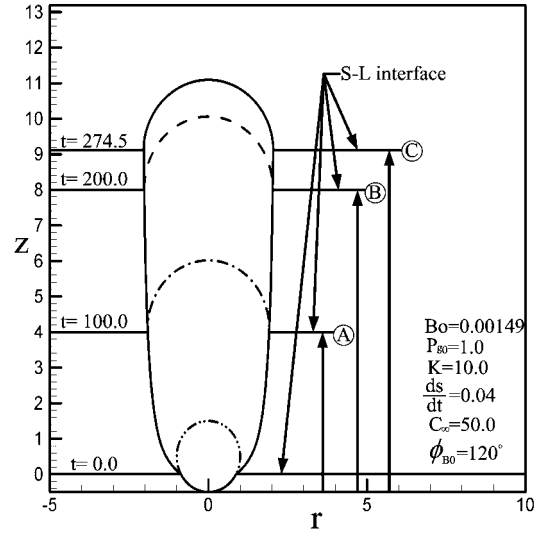


Fig. 5 A predicted development of pore shapes at different times

https://doi.org/10.1017/jmech.2012.1 Published online by Cambridge University Press

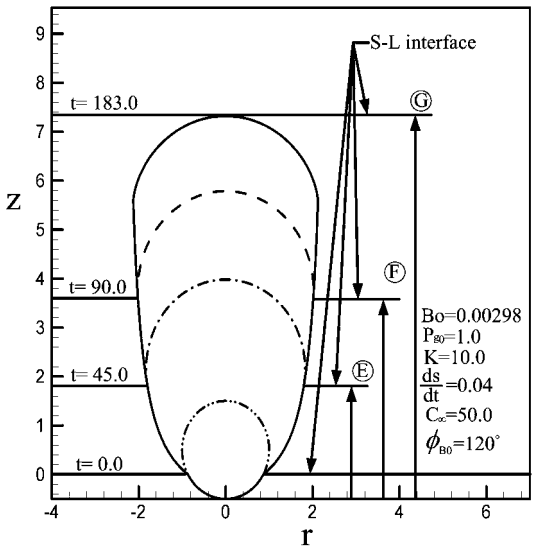


Fig. 6 A predicted development of pore shapes at different times

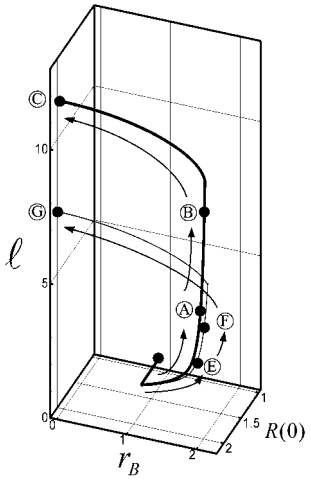


Fig. 7 Three-dimensional phase diagram to describe development of pore shapes for previous figures

5. CONCLUSIONS

In this study, an analytical model is provided to predict the general growth and entrapment of a microbubble as a pore in the solid during solidification. The model satisfies conservation of mass, momentum, energy and thermodynamic and physico-chemical equilibriums at the bubble surface. The development of the pore shapes in the solid can be uniquely described by a three-dimensional dimensionless phase diagram for a given initial Bond number. Since the predicted pore shape has been found to agree with experimental data, the present work can be successfully utilized to investigate more interesting and challenging topics for the development of the pore shape in solid.

REFERENCES

1. Devletian, J. H. and Wood, W. E., "Factors Affecting Porosity in Aluminum Welds—A Review," *Welding Research Council Bulletin*, **290**, pp. 1–18 (1983).
2. Kou, S., *Welding Metallurgy*, Wiley, New York (1987).
3. Zhao, H., White, D. R. and DebRoy, T., "Current Issues and Problems in Laser Welding of Automotive Aluminum Alloys," *International Materials Reviews*, **44**, pp. 238–266 (1999).
4. Ramirez, J. E., Han, B. and Liu, S., "Effect of Welding Variables and Solidification Substructure on Weld Metal Porosity," *Metallurgical Materials Transactions A*, **25**, pp. 2285–2294 (1994).
5. Kubo, K. and Pehlke, R. D., "Mathematical Modeling of Porosity Formation in Solidification," *Metallurgical Materials Transactions B*, **16**, pp. 359–366 (1985).
6. Lee, P. D., Chirazi, A. and See, D., "Modeling Microporosity in Aluminum-Silicon Alloys: A Review," *Journal of Light Metals*, **1**, pp. 15–30 (2001).
7. Hardin, R. and Beckermann, C., "Effect of Porosity on the Stiffness of Cast Steel," *Metallurgical and Materials Transactions A*, **38**, pp. 2992–3006 (2007).
8. Oliete, P. B. and Peña, J. I., "Study of the Gas Inclusions in $A_{l2}O_3/Y_3A_{l5}O_{12}$ and $A_{l2}O_3/Y_3A_{l5}O_{12}/ZrO_2$ Eutectic Fibers Grown by Laser Floating Zone," *Journal of Crystal Growth*, **304**, pp. 514–519 (2007).
9. Jamgotchian, H., Trivedi, R. and Billia, B., "Interface Dynamics and Coupled Growth in Directional Solidification in Presence of Bubbles," *Journal of Crystal Growth*, **134**, pp. 181–195 (1993).
10. Nakajima, H., "Fabrication, Properties and Application of Porous Metals with Directional Pores," *Progress in Materials Science*, **52**, pp. 1091–1173 (2007).
11. Chalmers, B., *How Water Freezes*, Scientific American, **200**, pp. 114–122 (1959).
12. Grigorenko, G. M., "Formation of Pores in Welds," *Avt Svarka*, **10**, pp. 12–17 (1970).
13. Wei, P. S., Huang, C. C. and Lee, K. W., "Nucleation of Bubbles on a Solidification Front-Experiment and Analysis," *Metallurgical Materials Transactions B*, **34**, pp. 321–332 (2003).
14. Bianchi, M. V. A. and Viskanta, R., "The Effect of Air Bubbles on the Diffusion-Controlled Solidification of Water and Aqueous Solutions of Ammonium Chloride," *International Journal of Heat Mass Transfer*, **42**, pp. 1097–1110 (1999).
15. Rodriguez, D. J. and Shedd, T. A., "Entrainment of Gas in the Liquid Film of Horizontal, Annular, Two-Phase Flow," *International Journal of Multiphase Flow*, **30**, pp. 565–583 (2004).
16. Cox, M. C., Anilkumar, A. V., Grugel, R. N. and Lee, C. P., "Effect of Step-wise Change in Processing Pressure on Isolated Pore Growth during

https://doi.org/10.1017/jmech.2012.1 Published online by Cambridge University Press

Controlled Directional Solidification in Small Channels," *Journal of Crystal Growth*, **311**, pp. 327–336 (2009).
17. Inada, T., Hatakeyama, T. and Takemura, F., "Gas-Storage Ice Grown Form Water Containing Mircobubbles," *International Journal of Refrigeration*, **32**, pp. 462–471 (2009).
18. Yoshimura, K., Inada, T. and Koyama, S., "Growth of Spherical and Cylindrical Oxygen Bubbles at an Ice-Water Interface," *Crystal Growth and Design*, **8**, pp. 2108–2115 (2008).
19. Liu, Y., Li, Y. X., Wan, J. and Zhang, H. W., "Evaluation of Porosity in Lotus-Type Porous Magnesium Fabricated by Metal/Gas Eutectic Unidirectional Solidification," *Materials Science and Engineering A*, **402**, pp. 47–54 (2005).
20. Park, J. S., Hyun, S. K., Suzuki, S. and Nakajima, H., "Effect of Transference Velocity and Hydrogen Pressure on Porosity and Pore Morphology of Lotus-Type Porous Copper Fabricated by a Continuous Casting Technique," *Acta Materialia*, **55**, pp. 5646–5654 (2007).
21. Tane, M. and Nakajima, H., "Influence of Ultrasonic Agitation on Pore Formation and Growth during Unidirectional Solidification of Water-Carbon Dioxide Solution," *Materials Transactions*, **47**, pp. 2183–2187 (2006).
22. Murakami, K. and Nakajima, H., "Formation of Pores during Unidirectional Solidification of Water Containing Carbon Dioxide," *Materials Transactions*, **43**, pp. 2582–2588 (2002).
23. Murakami, K., Nakai, Y. and Nakajima, H., "Direct Observation of Pore Growth in Unidirectionally Solidified Water-Carbon Dioxide Solution," *International Journal of Cast Metals Research*, **15**, pp. 459–463 (2002).
24. Geguzin, Ya. E. and Dzuba, A. S., "Crystallization of a Gas-Saturated Melt," *Journal of Crystal Growth*, **52**, pp. 337–344 (1981).
25. Wei, P. S., Huang, C. C., Wang, Z. P., Chen, K. Y. and Lin, C. H., "Growths of Bubble/Pore Sizes in Solid during Solidification -An In Situ Measurement and Analysis," *Journal of Crystal Growth*, **270**, pp. 662–673 (2004).
26. Wei, P. S., Kuo, Y. K., Chiu, S. H. and Ho, C. Y., "Shape of a Pore Trapped in Solid during Solidification," *International Journal of Heat Mass Transfer*, **43**, pp. 263–280 (2000).
27. Wei, P. S. and Ho, C. Y., "An Analytical Self-Consistent Determination of a Bubble with a Deformed Cap Trapped in Solid during Solidification," *Metallurgical Materials Transactions B*, **33**, pp. 91–100 (2002).
28. Wei, P. S. and Hsiao, C. C., "Microbubble or Pendant Drop Control Described by a General Phase Diagram," *International Journal of Heat Mass Transfer*, **52**, pp. 1304–1312 (2009).

(Manuscript received February 22, 2011,
accepted for publication April 22, 2011.)

https://doi.org/10.1017/jmech.2012.1 Published online by Cambridge University Press